Ultra High Energy Cosmic Rays & Super-heavy Dark Matter

Observables and prospect of (non)detection

Luca Marzola *1,2 and Federico R. Urban †2

Dated: 23rd November 2016

Abstract:

We reanalyse the prospects for upcoming Ultra-High Energy Cosmic Ray experiments in connection with the phenomenology of Super-heavy Dark Matter. We identify a set of observables well suited to reveal a possible anisotropy in the High Energy Cosmic Ray flux induced by the decays of these particles, and quantify their performance via Monte Carlo simulations that mimic the outcome of near-future and next-generation experiments. The spherical and circular dipoles are able to tell isotropic and anisotropic fluxes apart at a confidence level as large as 4σ or 5σ , depending on the Dark Matter profile. The forward-to-backward flux ratio yields a comparable result for relatively large opening angles of about 40 deg, but it is less performing once a very large number of events is considered. We also find that an actual experiment employing these observables and collecting 300 events at 60 EeV would have a 50% chance of excluding isotropy against Super-heavy Dark Matter at a significance of at least 3σ .

¹Laboratory of Theoretical Physics, Institute of Physics, University of Tartu; Ravila 14c, 50411 Tartu, Estonia.

²Laboratory of High Energy and Computational Physics, National Institute of Chemical Physics and Biophysics, Rävala pst. 10, 10143 Tallinn, Estonia.

^{*}luca.marzola@ut.ee

[†]federico.urban@kbfi.ee

1. Introduction

Keeping up with a long-standing tradition in the literature about "Dark Matter" (DM from now on), we kick off by sternly pointing out the major lacuna in our understanding of the Universe that the origin of DM is. In fact, measurements of the cosmic microwave background power spectrum and the rotation curves of galaxies, amongst others, suggest the existence of a new substance which behaves like ordinary matter as far as gravity is concerned [1,2]. The problem is that, unlike baryonic matter which aggregates in planets and stars, this mysterious material does not shine any light – hence the differently creative name of DM. Since nothing in the Standard Model of Particle Physics (SM in short) has the right properties to play the rôle of DM, these observations are regarded as a rather solid evidence for the existence of New Physics. DM has been a central problem for Physics in the latest four decades, as testified by the over 14.000 dedicated arXiv papers. The proposed DM candidates range from condensates of scalar fields that coherently oscillate according to their potential (axion/axion-like particles) [3] to sterile neutrinos or new fermions [4–6], including primordial black holes [7,8] and particles emerging from extensions of General Relativity [9–11].

This landscape of DM models, however, is not uniformly populated; because of the possible connections with Supersymmetric theories and the simplicity of its dynamics, one particular scenario of DM has been dominating the scene: Weakly Interacting Massive Particle (WIMP) DM [12,13]. Undoubtedly, the WIMP paradigm has had a profound impact on shaping the ongoing experimental physics program dedicated to DM searches. In spite of the extensive effort, however, so far no experiment has provided any evidence in support of WIMP DM. New data release are progressively relegating the models to unpleasant corners of their parameter spaces [14–17] and, with no supersymmetric particle detected at the LHC [18–21], the WIMP paradigm begins to crack and wither.

For this reason, in this paper we take a pragmatic step into the darkness of DM, focusing on a model that typically yields little signatures: Super-heavy DM (or SHDM to be original). The idea behind SHDM is that DM is composed by a gravitationally produced non-thermal relic of supermassive particles [22–26]. According to the present literature, SHDM with a mass scale $\mathcal{O}(10^{12}-10^{14})$ GeV could originate in Supersymmetry-breaking and Kaluza-Klein models [27–30], or Multi-Graviton theories [9–11], as well as in Coleman-Weinberg extensions of the SM in concomitance with inflation [31]. The weakness of gravitational interactions then explains the lack of any signal in direct detection experiment, whereas collider experiments would need to reach energies and luminosities significantly higher than those of current machines to probe the scheme. If SHDM particles are stable, there is no way for current and next-generation DM indirect detection experiments to prove their properties. Yet, Ultra High-Energy Cosmic Rays (UHECR) experiments may have something to say about (slowly) decaying SHDM¹.

If SHDM decays produce SM particles, it is not difficult to see that the amount of UHECR resulting from these processes should increase as we look toward SHDM denser regions, like the centre of our Galaxy. Consequently, it is possible to probe SHDM models with UHECR experiments by measuring anisotropies in the UHECR flux [36-40]. Motivated by this basic observation, we set out to find the best possible way to detect a SHDM signal via its features across the sky. In this paper, we thus introduce different observables aimed at revealing a possible anisotropic UHECR component and

¹A complementary approach to bound the properties of SHDM candidates consists in studying their impact on inflationary observables [32–34] and on the Cosmic Microwave Background Radiation [35].

quantify their performance via Monte Carlo (MC) simulations that capture the gist of current and next generation experiments. On top of that, we quantify the power of an experiment to reject the hypothesis of an isotropic UHECR flux against a predicted SHDM one through the best performing observables.

The paper is organised as follows: the next section offers an overview of the quantities relevant for UHECR physics and specifies the ingredients from SHDM which are present in our analyses. Section 3 describes our observables and presents the details of the simulation algorithms. The most important results of our work are presented in Section 4, whereas complementary ones are included in the Appendix. We close with Section 5.

2. An overview

The flux of UHECR that arrive on Earth with energy [E, E+dE] from an infinitesimal cone of aperture β centred on the direction \mathbf{n} can be generally decomposed into a galactic and an extragalactic components

$$J_{x}(E,\mathbf{n}) = J_{x}^{g}(E,\mathbf{n}) + J_{x}^{eg}(E,\mathbf{n}); \qquad x \in \{p,\nu,\gamma\}.$$

$$\tag{1}$$

Here x specifies the UHECR primary: p stands for protons, ν for neutrinos, and γ for photons. Throughout the following we take the corresponding fluxes J_x to be normalised in units of area, time, energy and solid angle. For simplicity, and also because that is what is expected from SHDM decays, we will disregard all baryons but protons, however it is straightforward to extend the present analysis to heavier nuclei.

The relative contribution of protons, neutrinos and other species to the detected (or expected) flux changes significantly depending on the energy range we observe. This behaviour is due to the interactions of the UHECR injected at the source with the cosmic background and intervening media [41–43]; for instance:

- protons with an energy roughly above 60 EeV (GZK limit [44,45]) scatter on the Cosmic Microwave Background photons and produce Δ resonances which decay into protons/neutrons and pions. The mean free path associated to this interaction is $\mathcal{O}(100)$ Mpc (GZK horizon).
- the mean free path of photons above the GZK limit is restricted to a few Mpc by interactions with the radio background.
- neutrinos are not affected by the cosmic backgrounds but they can hardly initiate the observed air showers due to their reduced cross sections on nucleons.

By comparing these limits with the average size of Galaxies $\mathcal{O}(100)$ kpc, the average distance of Galaxies in a cluster $\mathcal{O}(1)$ Mpc, and the average distance of clusters in superclusters $\mathcal{O}(10)$ Mpc, we understand how tiny we are and that UHECR detected with energy above the GZK cutoff are most likely charged nuclei generated in the local supercluster. Interestingly, the palatable astrophysical sources of UHECRs contained within the GZK horizon do not typically possess the right characteristics to accelerate these particles at the observed high energies [43, 46]. Another possibility is that UHECRs come from the decay of SHDM particles within our own Milky Way,

which is the idea we pursue here. Thus, in the following, we will assume that the UHECR flux is dominated by the decay products of local SHDM.

2.1. The galactic component

The galactic component of the flux is defined as

$$J_{x}^{g}(E,\mathbf{n}) = \frac{1}{4\pi} \int \mathcal{I}_{x}(E,r,\mathbf{n}) \, \mathrm{d}r; \qquad x \in \{p,\nu,\gamma\}$$
 (2)

where the 4π normalisation accounts for the isotropy of the DM decay processes, and r is our distance to the source located within the Milky Way. These are characterised by the intrinsic DM emissivity

$$\mathcal{I}_{x}(E, r, \mathbf{n}) = n_{DM}(r, \mathbf{n}) \frac{\mathsf{d}\Gamma_{x}}{\mathsf{d}E}$$
(3)

which depends on the galactic DM density profile, $n_{DM}(r, \mathbf{n})$ and on the specific DM interactions encapsulated in the differential decay widths $d\Gamma_x/dE$ into the particle species x.

The SHDM decay into hadrons is complicated by the hadronisation process. For instance, considering a specific hadron h, we have [47-49]

$$\frac{1}{\Gamma} \frac{\mathrm{d}\Gamma_h}{\mathrm{d}x} = \sum_a \int_x^1 \frac{1}{\Gamma_a} D_a^h(z, \mu^2) \frac{\mathrm{d}\Gamma_a(y, \mu^2, m_{DM}^2)}{\mathrm{d}y} \bigg|_{y=x/z} \frac{\mathrm{d}z}{z} \tag{4}$$

where m_{DM} is the SHDM mass that sets the energy scale of the decay process, $\Gamma := \sum_x \Gamma_x$ and in the integral x, y and z are various fractions of available maximum momentum and primary parton momentum carried by the hadron under scrutiny:

$$x \simeq 2 \frac{E_h}{m_{DM}}; \qquad z \simeq \frac{E_h}{E_a}; \qquad y = \frac{x}{z} \simeq 2 \frac{E_a}{m_{DM}}.$$
 (5)

Eq. (4) allows us to separate the details of hadronisations process from the fundamental properties of SHDM described in DM models. In fact, the former are contained in the *fragmentation function* $D_a^h(z,\mu)$ [47–49], which essentially corresponds to the probability that a process initiated by a parton a result in a specific hadron h. Notice that the while the fragmentation functions depend on the factorisation scale μ , the resulting differential branching ratio into hadron does not depend on this quantity. This forces the cancellation of the dependence on the factorisation scale order by order in perturbation theory amongst the terms on the right-hand side of the above equation, in a way that the fragmentation functions obey the so-called DGLAP equation [50–53]. Once the fragmentation functions are measured at the electroweak scale, we can use the DGLAP equation to evolve them up to the DM scale, where the relevant decay process takes place.

As the fragmentation functions are computed according to the above prescription, we can focus on the particle physics which regulates the remaining terms on the right-hand side of Eq. (4). In particular, the (exclusive) differential decay width of SHDM into a parton a can be computed as

$$d\Gamma_{a} = \frac{|\mathcal{M}_{a}|^{2}}{8\pi m_{DM}} \delta \left(m_{DM} - 2E_{a} \right) dE_{a} \quad \Longrightarrow \quad \frac{d\Gamma_{a}}{dE_{a}} = \frac{|\mathcal{M}_{a}|^{2}}{8\pi m_{DM}^{2}} \delta \left(1 - y \right) \tag{6}$$

and therefore

$$\frac{\mathrm{d}\Gamma_a}{\mathrm{d}v} = \frac{|\mathcal{M}_a|^2}{16\pi \, m_{DM}} \delta\left(1 - y\right) \,. \tag{7}$$

The integrated exclusive decay width then amounts to

$$\Gamma_a = \frac{1}{16\pi m_{DM}} |\mathcal{M}_a|^2 \tag{8}$$

where, throughout the computations, the squared matrix elements $|\mathcal{M}_a|^2$ are implicitly computed for the momenta as imposed by the energy-momentum conservation. Hence,

$$\frac{1}{\Gamma} \frac{d\Gamma_h}{dx} = \sum_a \int_x^1 \frac{1}{\Gamma_a} \frac{d\Gamma_a}{dy} D_a^h(z, \mu^2) \frac{dz}{z} = \sum_a \int_x^1 \delta\left(1 - \frac{x}{z}\right) D_a^h(z, \mu^2) \frac{dz}{z} = \sum_a D_a^h(x, \mu^2) \equiv \frac{dN_h}{dx}$$
(9)

with $D^p = D^p_q + D^p_g$ being the proton fragmentation function. The last equality holds after the singular fragmentation functions for quarks and gluons have been properly weighted by the relative color factors. Putting all together we then find

$$J_{X}^{g}(E, \mathbf{n}) = \frac{1}{4\pi} \int n_{DM}(r, \mathbf{n}) \frac{d\Gamma_{X}}{dE} dr = \frac{1}{4\pi\tau} \frac{1}{\Gamma} \frac{d\Gamma_{X}}{dE} \int n_{DM}(r, \mathbf{n}) dr =$$

$$= \frac{1}{4\pi\tau m_{DM}} \frac{dN_{X}}{dE} \int \rho_{DM}(r, \mathbf{n}) dr.$$
(10)

Notice that we define the Galactic flux on the whole sphere as $J_x^g(E) := \int_{4\pi} d\mathbf{n} J_x^g(E, \mathbf{n})$.

2.2. The extragalactic component

Given our preliminary discussion at the beginning of the section, it is clear that the extragalactic contribution amounts prevalently to an isotropic neutrino flux with a subdominant proton component, at least at the highest energies we are interested in. Notice that although neutrinos are very hard to detect by current ground observatories, the high-energy neutrino flux detected in dedicated experiments can still be used to set the magnitude of the extragalactic component of the UHECR [54–56].

The extragalactic proton flux can itself be divided in two components: the first is the almost isotropic low-energy proton flux as measured in running experiments, which we take to follow a broken power-law spectrum:

$$J_{p}^{exp}(E) = \frac{1}{4\pi} J_{1} \begin{cases} E^{-\gamma_{1}} & 1 \text{ EeV} \leq E < E_{\text{ankle}} \\ E_{\text{ankle}}^{\gamma_{2}-\gamma_{1}} E^{-\gamma_{2}} & E_{\text{ankle}} \leq E < E_{GZK} \\ E_{\text{ankle}}^{\gamma_{2}-\gamma_{1}} E_{GZK}^{\gamma_{3}-\gamma_{2}} E^{-\gamma_{3}} & E > E_{GZK} \end{cases} , \tag{11}$$

where J_1 is the total flux normalisation at 1 EeV, $E_{\rm ankle} \approx 5$ EeV is the first break (ankle) and $E_{GZK} \approx 54$ EeV is the GZK cutoff as measured by Telescope Array [57–59]; the powers are $\gamma_1 = 3.3$, $\gamma_2 = 2.7$, and $\gamma_3 = 4.6$ — similar results are obtained by the Pierre Auger [60, 61] observatory. This flux decays much more rapidly than the expected flux from SHDM, and is only relevant at low energies (up to and around the GZK cutoff).

The second extragalactic proton component comes from SHDM itself. If we neglect the effect of redshift (which is a very well justified assumption) we expect the flux

$$J_{p}^{eg}(E) = \frac{1}{4\pi} \frac{R_{GZK}}{m_{DM}\tau} \overline{\rho}_{DM} \frac{dN_{x}}{dE}$$
 (12)

where R_{GZK} is the physical particle horizon from which the vast majority of the flux comes from (the GZK horizon) and $\bar{\rho}_{DM}:=\Omega_m\rho_c$ with $\Omega_m=0.23$ the DM fraction of the critical energy density $\rho_c=1.1\times 10^{-5}h_0^2$ GeV/cm³, and $h_0=0.67$ [62].

To obtain a rough estimate of the relative weight between galactic and extragalactic contributions in the proton flux, we consider the ratio of the two fluxes on the sphere:

$$\frac{J_p^{eg}(E)}{J_p^g(E)} \approx \frac{4\pi R_{GZK} \bar{\rho}_{DM}}{\int d\Omega dr \rho_{DM}} \approx 2.5 \times 10^{-2}$$
 (13)

where we used $R_{GZK}=100$ Mpc; for the local density ρ_{DM} we took the Navarro-Frenk-White profile (see below for details). One can also easily show that even when looking towards the Galactic anticentre, the local DM contribution is about a factor of 10 stronger than the cosmological contribution. Similar figures hold for the photon fluxes as well². This rough estimate also makes it clear that redshift effects can safely be neglected at energies above the GZK cutoff when considering photons and proton fluxes.

Neutrinos, on the other hand, do not possess a GZK horizon, and this implies that galactic and extragalactic fluxes are comparable at all energies. To estimate the extra-Galactic neutrino flux we use the result in [63]

$$J_{\nu}^{eg}(E) = \frac{1}{4\pi} \frac{\overline{\rho}_{DM}}{m_{DM}\tau} \int_{0}^{z_{cut}} dz \left| \frac{dt}{dz} \right| \frac{dN_{\nu}}{dE} \bigg|_{(1+z)E} e^{-S_{\nu}(E,z)}$$
(14)

where

$$\frac{\mathrm{d}t}{\mathrm{d}z} = -H_0(1+z)\sqrt{(1+z)^3\Omega_m + \Omega_\Lambda}; \tag{15}$$

and the neutrino opacity can be approximated at high redshift as

$$S_{\nu}(E,z) = \begin{cases} 3.5 \times 10^{-11} (\Omega_m h_0^2)^{-1/2} (1+z)^{5/2} (E/\text{EeV}) \times 10^{-3}, & 1 \ll z \lesssim z_{eq} \\ 0.81 \times 10^{-8} (1+z)^2 (E/\text{EeV}) \times 10^{-3}, & z \gtrsim z_{eq} \end{cases}$$
(16)

with $z_{eq}=3360$, the redshift at matter-radiation equality, and $\Omega_{\Lambda}=1-\Omega_{m}$. The actual calculation of the neutrino flux is quite involved, but for our purposes it suffices to say that it amount to about a tenth of the total flux; in practice, we can write $J_{\nu}^{eg}(E)=\kappa J_{\rho}^{g}(E)$ with $\kappa\approx0.1$.

2.3. Reconstructing the total flux

The total flux of UHECR can now be computed by summing over all particle species $x = \{p, \nu, \gamma\}$.

$$J_{tot}(E, \mathbf{n}) = J_{p}^{exp}(E) + J_{p}^{eg}(E) + J_{\gamma}^{eg}(E) + J_{\nu}^{eg}(E) + J_{p}^{g}(E, \mathbf{n}) + J_{\gamma}^{g}(E, \mathbf{n}) + J_{\nu}^{g}(E, \mathbf{n}), \quad (17)$$

²It is possible to refine the estimate by including a geometric factor that accounts for the distribution of DM in the halo. For the usual DM profiles considered in the literature this correction amounts to an $\mathcal{O}(1)$ coefficient.

where we can neglect the photon's and proton's extragalactic fluxes $J_p^{eg}(E)$ ans $J_{\gamma}^{eg}(E)$ as per our discussion above. In Eq. (17) all terms but $J_p^{exp}(E)$ are due to SHDM decays; $J_p^{exp}(E)$ instead is the measured flux which dominates below the GZK cutoff (in this scenario).

We keep the low-energy flux in order to properly normalise the number of events at low energy. Under the assumption that the galactic fluxes amount to the SHDM decay products we therefore have that

$$\frac{J_x^g(E,\mathbf{n})}{J_y^g(E,\mathbf{n})} \equiv \frac{D^x(E)}{D^y(E)}; \qquad x, y \in \{p, \nu, \gamma\}$$
 (18)

as the whole angular dependence enters through the line of sight integral which is common to both numerator and denominator.

Precise studies of the fragmentation function (see [48] and references therein) reveal that at the relevant energies $D^{x}(E) \propto E^{-1.9}$ independently of the species x. Hence, we can write $D^{x}(E) = A_{x}(E/\hat{E})^{-1.9}$ where $[A_{x}] = [E^{-1}]$, \hat{E} is the reference energy for the normalisation of the spectrum, and rather generically [48]:

$$\frac{A_{\gamma}}{A_{\rho}} = 2 \div 3, \qquad \frac{A_{\nu}}{A_{\rho}} = 3 \div 4. \tag{19}$$

Because of the behaviour of the fragmentation functions we can then write

$$J_{tot}(E, \mathbf{n}) = J_p^{e \times p}(E) + J_{\nu}^{eg}(E) + \left(1 + \frac{A_{\gamma}}{A_p} + \frac{A_{\nu}}{A_p}\right) J_p^g(E, \mathbf{n})$$
(20)

where

$$J_p^g(E, \mathbf{n}) = \underbrace{\frac{A_p}{4\pi m_{DM} \tau}}_{:=\hat{J}_p^{DM}} \left(\frac{E}{\hat{E}}\right)^{-1.9} \int \rho_{DM}(r, \mathbf{n}) \, \mathrm{d}r$$
 (21)

and
$$[\hat{J}_{x}^{DM}] = [E^{-2}t^{-1}].$$

We write the integral flux of photons, assumed to originate from SHDM decay, as

$$\Phi_{\gamma}^{DM}(E_{\text{cut}}) := \frac{1}{4\pi} \int_{E_{\text{cut}}}^{\infty} dE J_{\gamma}^{g}(E) =$$

$$= \frac{A_{\gamma}}{A_{p}} \hat{J}_{p}^{DM} \int_{E_{\text{cut}}}^{\infty} dE \left(\frac{E}{\hat{E}}\right)^{-\gamma} \underbrace{\int_{4\pi} d\mathbf{n} d\mathbf{r} \, \rho_{DM}(\mathbf{r}, \mathbf{n})}_{:=\omega}$$

$$= \frac{E_{\text{cut}}}{\gamma - 1} \left(\frac{E_{\text{cut}}}{\hat{E}}\right)^{-\gamma}$$

$$= \frac{E_{\text{cut}}}{\gamma - 1} \left(\frac{E_{\text{cut}}}{\hat{E}}\right)^{-\gamma}$$
(22)

with $\gamma=1.9$. As the ratios of $A_{\rm x}$ factor are known quantities, we can use the experimental limits on the integral photon flux [64–68] to bound the value of \hat{J}_p^{DM} . In particular, the strongest bound on the integral γ -flux Φ_{γ}^{DM} [67] constrains the relative SHDM contribution to be 2% above the energy of $E_{\rm cut}=10^{10}$ GeV (10 EeV), see Table 1.

Accounting for the experimental bound then implies

$$\Phi_{\gamma}^{DM}(E_{\text{cut}}) \lesssim \epsilon_{\gamma} \Phi^{exp}(E_{\text{cut}}) \implies \hat{J}_{p}^{DM} \lesssim \frac{\gamma - 1}{A_{\gamma}/A_{p}} \frac{1}{E_{\text{cut}} \omega} \left(\frac{E_{\text{cut}}}{\hat{E}}\right)^{\gamma} \epsilon_{\gamma} \Phi^{exp}(E_{\text{cut}}) \tag{23}$$

	Auger						TA		
E _{cut} [EeV]									
ϵ_{γ} [%]	0.4	0.5	1.0	2.6	2.0	5.1	31	6.2	29

Table 1: Upper bounds on the fraction of photons with respect to the total UHECR integral flux at a given energy from [64–68].

where $\Phi^{exp}(E_{\text{cut}})$ is the experimental integral spectrum, i.e., the total number of events detected by an experiment per unit of area steradians and time with an energy of E_{cut} or greater. Let us remark that this is a "best case scenario", that is, we directly employ the maximal SHDM flux currently allowed by observations.

All together, the flux from the direction \mathbf{n} is given by

$$J_{tot}(E, \mathbf{n}) = J_p^{e \times p}(E) + \kappa J_p^{eg}(E) + \left(1 + \frac{A_{\gamma}}{A_p} + \frac{A_{\nu}}{A_p}\right) J_p^g(E, \mathbf{n}), \qquad (24)$$

which integrated from a given threshold energy E_{cut} gives the total integral flux $\Phi_{tot}(E_{\text{cut}}, \mathbf{n})$.

3. Methodology

3.1. Dark Matter profiles

In order to explicitly compute the UHECR flux coming from SHDM decays we need to specify the SHDM density in our Galaxy. As at the time of writing a number of different DM profiles is still compatible with the observations, we have run our analysis for the most common ones (see [69]), and present here only two bracketing cases which give us the largest and smallest anisotropy. These respectively are the Einasto profile [70]:

$$\rho_{DM}(r_g) = \rho_* \exp\left\{-\frac{2}{\alpha} \left[\left(\frac{r_g}{r_*}\right)^{\alpha} - 1 \right] \right\}, \tag{25}$$

with $r_*=35.24$ kpc, $\alpha=0.11$ and $\rho_*=0.021$ GeV/cm³ and the Navarro-Frenk-White (NFW) profile [71]:

$$\rho_{DM}(r_g) = \rho_* \frac{r_*}{r_g} \left(1 + \frac{r_g^2}{r_*^2} \right)^{-2} , \qquad (26)$$

with $r_*=24.42$ kpc, and $\rho_*=0.184$ Gev/cm³. Notice that here we used galacto-centric coordinates where $r_g^2=(x-R_\odot)^2+y^2+z^2$ with (x,y,z) the Cartesian set centred on the Earth — in our numerical computations we also cut off the Galactic halo at 100 kpc.

3.2. Observables

There are a number of different ways to look for an anisotropic signal in the sky. In our case we expect a sharp peak in the flux in the area around the Galactic centre with respect to the Galactic

anticentre. Assuming we have access to the entire celestial sphere, the two most logical observables one can construct from the events collected within a given solid angle are the ratio and difference of the forward and backward (integral) fluxes from a given cone of aperture β . The ratio $r_{\rm fw/bw}$ is defined as:

$$r_{\text{fw/bw}} := \frac{\Phi_{\text{forward}}(E_{\text{cut}}, \beta)}{\Phi_{\text{backward}}(E_{\text{cut}}, \beta)}, \tag{27}$$

where $\Phi(E_{cut}, \beta) := \int_0^\beta d\mathbf{n} \Phi(E_{cut}, \mathbf{n})$ and "forward" and "backward" refer to the direction of the cone with respect to the Galactic centre. The difference instead is defined as:

$$d_{\mathsf{fw/bw}} := \frac{\Phi_{\mathsf{forward}}(E_{\mathsf{cut}}, \beta) - \Phi_{\mathsf{backward}}(E_{\mathsf{cut}}, \beta)}{\Phi_{\mathsf{forward}}(E_{\mathsf{cut}}, \beta) + \Phi_{\mathsf{backward}}(E_{\mathsf{cut}}, \beta)}. \tag{28}$$

Like we said, these definitions assume that one single experiment (or a cross-calibrated combination of more than one [72, 73]) is able to collect events from the entire celestial sphere. In reality, for current Earth-bound experiments it is typically possible to only see a limited region in the sky: variations on the previous definitions which can be used in this case are

$$r_{\text{fw/np}} \equiv \frac{\Phi_{\text{forward}}(E_{\text{cut}}, \beta)}{\Phi_{\text{north}}(E_{\text{cut}}, \beta)}, \qquad (29)$$

where the second cone is centred on the north (or south) Galactic poles, and similarly for $d_{\text{fw/np}}$. Since these combinations are not as sensitive as the forward/backward options, and since we have in mind future experiments with full-sky coverage, we will focus on Eq. (27) in what follows. The results obtained for (28) and the alternative definitions à la (29) are presented in Appendix.

Another convenient way to test for the presence of a possible anisotropy in a spherical sky distribution is to decompose it in spherical harmonics. Indeed, as any angular distribution on the unit sphere, the UHECR integral flux $\Phi(\mathbf{n})$ in a given direction \mathbf{n} can be decomposed in (real) spherical harmonics $Y_{\ell m}(\mathbf{n})$ as

$$\Phi(\mathbf{n}) = \sum_{\ell > 0} \sum_{m = -\ell}^{\ell} a_{\ell m} Y_{\ell m}(\mathbf{n}).$$
(30)

Turning this around we obtain the harmonic coefficients

$$a_{\ell m} := \int d\mathbf{n} Y_{\ell m}(\mathbf{n}) \Phi(\mathbf{n}). \tag{31}$$

From the $a_{\ell m}$ coefficients one can define a direction-independent angular power spectrum C_ℓ :

$$C_{\ell} := \frac{1}{2\ell + 1} \sum_{m=-\ell}^{\ell} |a_{\ell m}|^2 .$$
 (32)

The quantities $4\pi C_{\ell}$ characterise the amplitude (squared) of a relative flux deviation from an isotropic sky. Likewise, one can focus on a similar decomposition but in a single coordinate (for example right ascension α), defining the harmonic coefficients on a circle as

$$a_n := \frac{1}{2} \int d\mathbf{n} \Phi(\mathbf{n}) Y_n(\alpha) , \quad \text{with } Y_n(\alpha) := \frac{1}{\sqrt{2\pi}} \left\{ \sqrt{2} \cos n\alpha, 1, \sqrt{2} \sin |n| \alpha \right\}$$
 (33)

for $\{n > 0, n = 0, n < 0\}$, respectively. Similarly to the 3-dimensional case, the relative deviation from isotropy (squared) is characterised by

$$c_n^2 := \frac{1}{2} \left[(a_n)^2 + (a_{-n})^2 \right],$$
 (34)

which is the direction-independent combination³.

Notice that for the energies we are concerned with here (above the GZK cutoff), the impact of the Galactic magnetic field, as well as of the possible extragalactic field (yet unknown, but bounded from above [75, 76], is very limited and can be disregarded. Indeed, a proton travelling through the Milky Way at 60 EeV would be deflected by at most a few degrees, see for instance [77], and since the smallest aperture we consider is 5 deg, we can ignore this issue (the more so at higher energies).

3.3. Procedure

Our method is as follows. First of all, we choose the total number of events $N_{\rm ev}^{60}$ on the sphere at 60 EeV. The total number of events above a different energy is then given by the theoretical flux (24). We are typically interested in energies of 60 EeV and above, so we will work with 100, 300, and 500 events at this energy, with 300 being our "realistic" baseline value. In [78] it was found that the new planned JEM-EUSO space observatory should be able to deliver $N_{\rm ev}=250$ (580) events with $E\geq 80$ EeV within a few years of operation to reach a total exposure of 3×10^5 km²sr yr (today's experiments hover around an order of magnitude less than this, but only cover a part of the sky) for the absolute energy normalisation of the Pierre Auger Observatory or Telescope Array. At 100 EeV these numbers become 100 and 260, respectively.

We then compute the theoretical expectations for all of our observables. In the case of $r_{\rm fw/bw}$ and $d_{\rm fw/bw}$ we consider opening angles ranging from 5 deg to 90 deg in steps of 5 deg. We also vary the threshold energy from 60 EeV up to 1000 EeV for all observables.

After that, we obtain our errors from MC 10^6 isotropic simulations with $N_{\rm ev}^{60}$ events. We perform as many simulations as it is needed in order for our MC errors to result from the actual number counting fluctuations rather than from artefacts due to limited number of simulations. In the end we compute the confidence level at which an ideal experiment with $N_{\rm ev}^{60}$ detected events at 60 EeV would be able to discriminate between isotropic and anisotropic fluxes by employing our observables; this confidence level is a measure of the performance of said observables. This is our first result.

Secondly, in order to quantify the actual potential for a real experiment to reject isotropic flux over a flux generated by SHDM decay, we need to go one step further. Since we are interested in excluding an isotropic flux, we compute the means and standard deviations of 10^5 MC simulations with a given number of events under the hypothesis that the flux is given by SHDM decay, which gives us a mean \bar{X}_{SHDM} and a standard deviation σ_{SHDM}^X . Then we generate another set of 10^5 MC sets assuming an isotropic flux, and take the median X_{ISO} of a given observable. Finally, by looking at the distance in terms of standard deviations from the SHDM mean, that is $\mathcal{N}_{\sigma}^{50\%} = (\tilde{X}_{\text{ISO}} - \bar{X}_{\text{SHDM}})/\sigma_{\text{SHDM}}^X$, we quantify the minimum significance at which a single experiment would be able to reject the hypothesis of isotropic UHECR distribution in 50% of the cases, see [79] for more details on this approach.

³In the case of a real experiment the flux we observe is in fact the convolution of the actual flux times the experiment's exposure: this needs to be deconvolved in order to extract the true spherical harmonics [72–74]. This can always be done numerically provided that the exposure is known, hence we do not discuss the matter any further and assume here a uniform exposure.

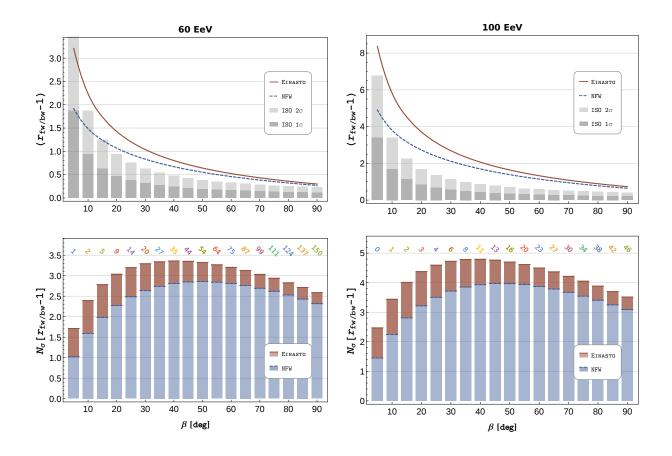


Figure 1: Performance of $(r_{\text{fw/bw}} - 1)$ for $N_{\text{ev}}^{60} = 300$; see the text for details.

4. Results

In Figure 1, top panels, we present the expected theoretical $(r_{\rm fw/bw}-1)$ for the two profiles NFW — Eq. (26) — and Einasto — Eq. (25) — for varying opening angle β in solid red and dashed blue, respectively, and the 1σ and 2σ dispersions around zero, which is the mean value expected from an isotropic distribution in dark and light grey, respectively. We perform this analysis for threshold energies of 60 EeV (left panels) and 100 EeV (right panels). The bottom panels show the performance of the $(r_{\rm fw/bw}-1)$ observable in telling isotropy and SHDM apart again for NFW and Einasto profiles in solid red and dashed red, respectively; this perfomance is calculated as the distance between the theoretical SHDM and isotropic values in number of sigmas. The total number of events on the sphere above 60 EeV is 300; this number reduces to 92 above 100 EeV. For reference, the (rounded) number of events expected for an isotopic distribution within a solid angle with opening β is also included in the bottom panel over the histograms.

The results in Figure 1 then indicate that the opening angles most suitable for detecting possible deviations in the UHECR flux from isotropy, in the context of SHDM decay products, are intermediate values around 40 deg. Indeed, for smaller β the ratio between forward and backward fluxes increases dramatically, but the number of events decreases and the fluctuations become very large, especially since the overall number of events is quite small (only 92 at 100 EeV). On the other hand, at very large β even though we collect more statistics, the signal is diluted by a factor of about 10 with respect to the theoretical prediction for $(r_{\rm fw/bw}-1)$ at 5 deg and 90 deg. At its

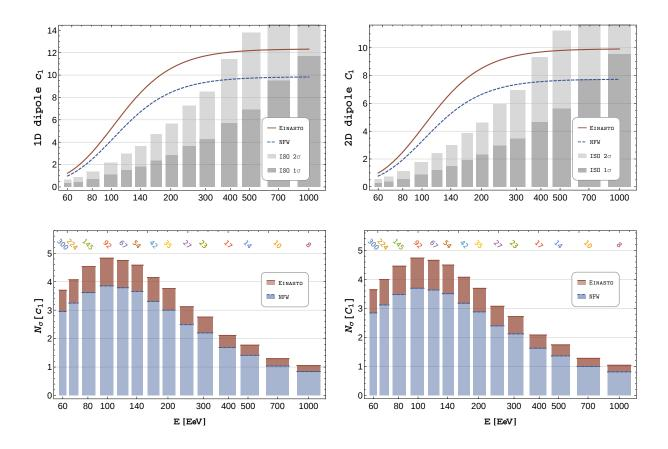


Figure 2: Performance of the 1D dipole c_1 (left) and 2D one C_1 (right) for $N_{\rm ev}^{60}=300$; see the text for details.

best, this observable can potentially tell SHDM apart from isotropy at a significance of about 3σ for a 60 EeV cutoff, and up to about 4σ – 5σ by picking only events above 100 EeV, where $J_p^{exp}(E)$ is negligible and the SHDM flux fully dominates. For higher energies the ratio of fluxes saturates as above 100 EeV only the SHDM flux is present; however, the overall statistics rapidly degenerates and the signal is bogged down by low statistics.

In Figure 2, top panels, we present the expected theoretical one-dimensional, or circular (along right ascension), dipole c_1 (left) and two-dimensional, or spherical, dipole C_1 once again for the two profiles Eq.s (26) and (25) in solid red and dashed blue, respectively, for different energy thresholds $E_{\rm cut} = \{60, 67, 80, 100, 120, 140, 170, 200, 250, 300, 400, 500, 750, 1000\}$ EeV. In the same plots we include the histograms of the 1σ and 2σ dispersions around zero in dark and light grey, respectively. The bottom panels, similarly to Fig. 1, show the performance of the 1D and 2D dipoles to tell isotropy and SHDM apart again for NFW and Einasto profiles in solid red and dashed red, respectively. For reference, the total (rounded) number of events is also included in the bottom panel over the histograms — notice how the number of events drops to a total of only 23 events already at 300 EeV.

These results demonstrate that the best threshold energy for the rejection of the isotropic hypothesis against a SHDM-driven local flux is around 100 EeV, as anticipated above. At this energy the dipoles can distinguish between these two hypotheses at a significance of about 4σ (5σ) for

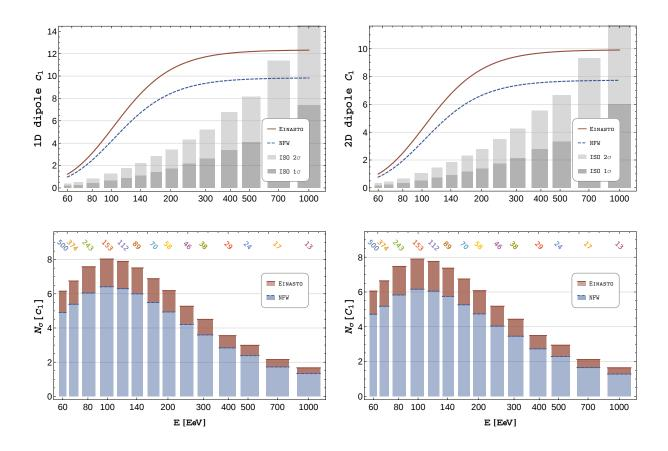


Figure 3: Performance of the 1D dipole c_1 (left) and 2D one C_1 (right) for $N_{\rm ev}^{60}=500$; see the text for details.

an NFW (Einasto) SHDM profile. At higher energies the overall dipole magnitude reaches a plateau, but as $N_{\rm ev}$ rapidly shrinks, the performance of the dipoles worsens significantly (see the top panels).

In Fig. 3 we show how the expected sensitivities change when $N_{\rm ev}^{60}$ raises up to 500. The peak sensitivities rise from around 4σ for our baseline $N_{\rm ev}^{60}=300$ up to the $6\sigma-8\sigma$ range with as many as 500 events. The peak sensitivities are as usual reached around 100 EeV, since, like we mentioned in the main text, from this point on the SHDM flux completely dominates, so the anisotropy does not grow anymore; on the other hand at higher energies the overall number of events reduces, boosting the counting errors. It is interesting to see how the spherical harmonics, capitalising on the maximal number of events, become much more sensitive than "geometric" observables such as the ratio $(r_{\rm fw/bw}-1)$ and the difference $d_{\rm fw/bw}$; for these quantities a small cone/cup means small statistics, but a large one significantly dilutes the effect, for there is no weighting of the directions (as instead is the case for the spherical harmonics) — we collect all further results for these quantities in the Appendix.

All together, we find that the dipoles and the forward-to-backward ratio are the strongest observables among the ones we have introduced in Sec. 3.2 at $N_{\rm ev}^{60}=300$; the harmonics however overpower the forward-to-backward ratio with larger datasets; we dig more in detail and present results for all other observables as well as the impact of $N_{\rm ev}^{60}$ in the Appendix.

		NFW		Eina	asto
$E_{\rm cut}$ [EeV]	$N_{\rm ev}$	c_1	C_1	c_1	C_1
60	300	2.6	2.9	2.6	3.0
67	224	2.7	3.1	2.8	3.2
80	146	3.0	3.4	3.0	3.4
100	92	3.2	3.8	3.2	3.7
120	67	3.3	4.0	3.3	3.8
140	54	3.4	4.1	3.3	3.8
170	42	3.3	4.0	3.2	3.8
200	35	3.2	3.9	3.1	3.7
250	27	3.0	3.6	2.8	3.4
300	23	2.8	3.4	2.7	3.2
400	17	2.5	3.0	2.4	2.8
500	14	2.2	2.7	2.1	2.5
700	700 10		2.3	1.8	2.1
1000	8	1.7	2.0	1.6	1.9

Table 2: Potential $\mathcal{N}_{\sigma}^{50\%}$ for a single experiment to observe departure from isotropy via the 1D and 2D dipoles, in terms of the confidence with which such hypothesis would be rejected in half of such experiments.

As promised, we also report the actual power for a real experiment to *reject isotropic flux over a flux generated by SHDM decay* for the strongest observables we identified, that is, the dipoles of Fig. 2. The values of $\mathcal{N}_{\sigma}^{50\%}$, that quantify the minimum confidence level at which an experiment can reject the isotropic flux hypothesis, are collected in Table 2. Once again, we can see that the most favourable energies are intermediate ones, around 100 EeV to 150 EeV.

5. Conclusion

In this paper we discussed the future prospects for the detection of an anisotropic UHECR flux generated by SHDM decays. After having identified observables tailored to test the hypothesis of an isotropic UHE proton flux, we assessed their potential via MC simulations that spans the reach of near-future and next-generation experiments, in the best case scenario for which the SHDM flux is maximal. The strongest observables are the 1D and 2D harmonic dipoles (the 1D dipole is obviously along right ascension), and the forward-to-backward ratio. These quantities can potentially discriminate between isotropic and anisotropic fluxes at the 4σ to 5σ confidence level for NFW and Einasto SHDM profiles, respectively. The best values hold for an energy cutoff at (and around) 100 EeV, and, in the case of ($r_{\rm fw/bw}-1$), for opening angles around 40 deg — smaller angles suffer from a sharp decrease in statistics. As the total number of events $N_{\rm ev}^{60}$ grows, the spherical harmonics tend to outperform the other observables. Finally, we would like to remark that, given a measurement of a dipole, the entire harmonic power spectrum can be predicted: higher multipoles, albeit less pronounced, can therefore be utilised to discern the SHDM origin of a potential anisotropic flux component.

Moreover, we have also quantified the power of a single experiment to reject the isotropy hypothesis

by employing our best observables. In this regard we find that, by looking at the integral flux above 100 EeV, the significance at which the isotropic flux hypotesis can be refuted exceeds the 3σ level in at least 50% of the cases.

To conclude, UHECR experiments do possess a significant potential to test models of SHDM, the phenomenology of which is not accessible at collider and direct detection experiments. Our results can be used straightforwardly within concrete SHDM models to derive distinguishing features that can potentially by observed in the upcoming UHECR sky.

Acknowledgements

LM acknowledges the Estonian Research Council for supporting his work with the grant PUTJD110; FU was supported by the ERC grant PUT808 and the ERDF CoE program. The authors thank Lucia Perrini and Antonio Racioppi for useful discussions, and Andrew Fowlie and Peter Tinyakov for reading the draft. This paper is dedicated to the memory of the Speakeasy, in Tallinn, where most of this work was conceived.

Appendix: all the rest

In addition to the $(r_{\rm fw/bw}-1)$ ratio of Eq. (27) shown in Figure 1, an alternative way to look for a forward/backward flux anisotropy is to use the difference $d_{\rm fw/bw}$ from Eq. (28). In Fig. 4 we show the performance of this observable for the $N_{\rm ev}^{60}=300$. The panels are organised in the same way as in Fig. 1 and show that this quantity is not as sensitive as the ratio $(r_{\rm fw/bw}-1)$, reaching at most the 2.5σ level.

If an experiment does not have access to the forward and backward regions of the sky, one may be forced to pick instead observation cones centred towards north (or south, or even left and right which are all equivalent given the spherical symmetry of the DM density distribution). In Figs. 5 and 6 we show the two "geometric" observables $(r_{\rm fw/np}-1)$ and $d_{\rm fw/np}$ using the Galactic North Pole as the "background" counting region. Again, we take $N_{\rm ev}^{60}=300$, and the panels are organised in the same way as in Fig. 1. The $(r_{\rm fw/np}-1)$ is of course less sensitive compared to the $(r_{\rm fw/bw}-1)$, as is expected since a cone towards the Galactic North Pole encompasses more SHDM by volume than a corresponding cone pointing backward from the Galactic Centre. It is also interesting to notice how the effect of the cross-correlation between forward and north cones washes out (as it should) the sensitivity to the anisotropy, as the cones overlap beyond 45 deg. The $d_{\rm fw/np}-1$ is even less sensitive, see Fig. 6.

To get a grip on the dependence of the "geometric" observables on the overall number of events, we have performed our simulations with $N_{\rm ev}^{60}=100$ and $N_{\rm ev}^{60}=500$, and the results for $(r_{\rm fw/bw}-1)$ are presented in Figs. 7 and 8, respectively. With only 100 events the sensitivity is down to $1.5\sigma-2\sigma$ for a 60 EeV cutoff, and around 2.5σ at 100 EeV, down from around 3σ at 60 EeV and $4\sigma-5\sigma$ with the 100 EeV cutoff.

On the other hand, when $N_{\rm ev}^{60}=500$, such as it may be expected from the new space-borne

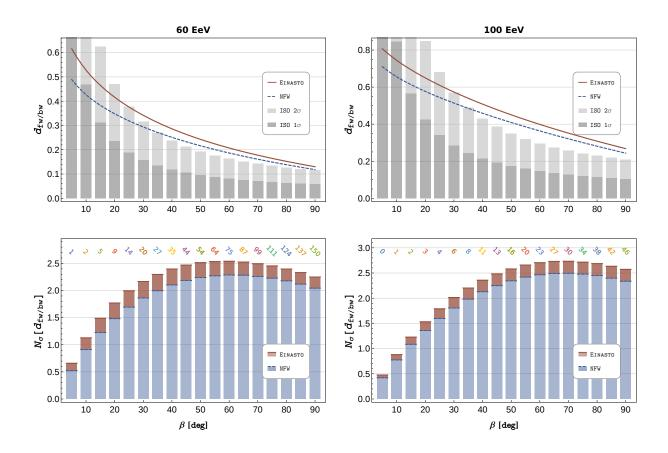


Figure 4: Performance of $d_{\rm fw/bw}$ for $N_{\rm ev}^{60}=300$; see the text for details.

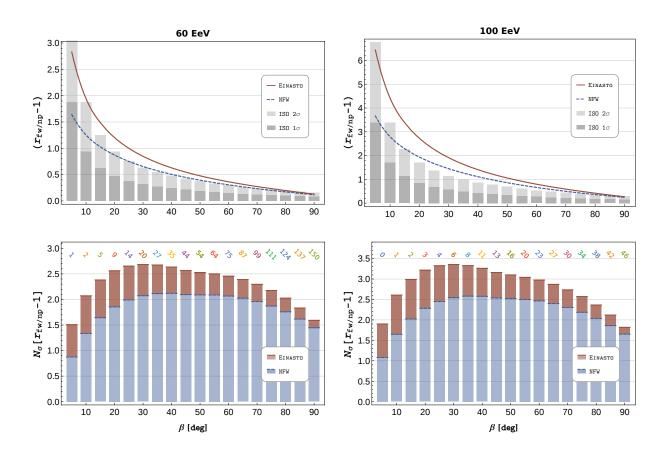


Figure 5: Performance of $(r_{\rm fw/np}-1)$ for $N_{\rm ev}^{60}=300$; see the text for details.

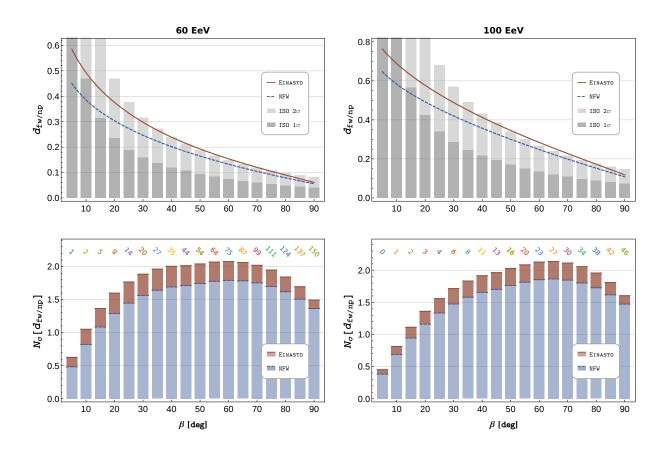


Figure 6: Performance of $d_{\mathrm{fw/np}}$ for $N_{\mathrm{ev}}^{60}=300$; see the text for details.

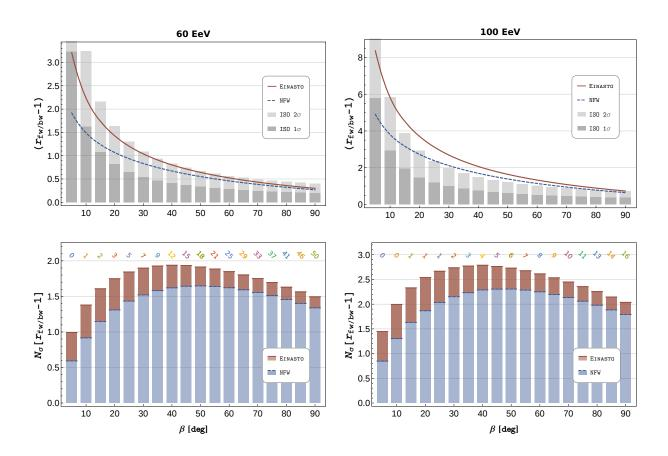


Figure 7: Performance of $(r_{\rm fw/bw}-1)$ for $N_{\rm ev}^{60}=100$; see the text for details.

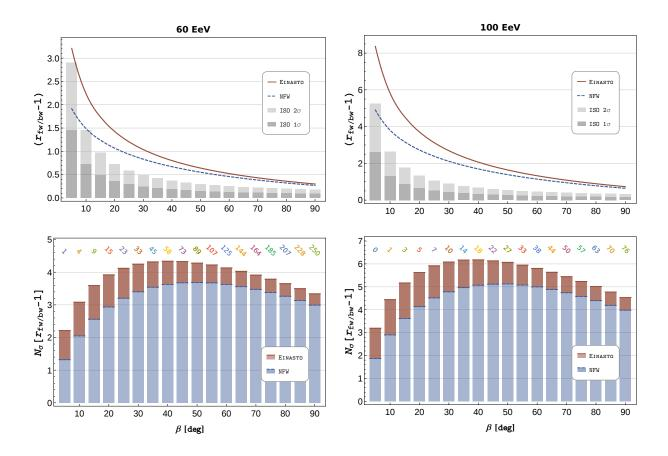


Figure 8: Performance of $(r_{\text{fw/bw}} - 1)$ for $N_{\text{ev}}^{60} = 500$; see the text for details.

UHECRs observatory JEM-EUSO, we would be able to attain a 5σ - 6σ discrimination between an isotropic distribution and a SHDM decay scenario following a NFW and an Einasto profiles, respectively, by placing a cutoff for the integral flux at 100 EeV. The quantity $(r_{\rm fw/bw}-1)$ is the most sensitive, that is, yields the best results in terms of the balance between statistics and expected signal strength, again at around 40 deg. Notice that despite the sensitivity of the forward-to-backward ratio grows with the number of events, it does so slower than the dipoles (for the same total number of events), see Fig. 3, which therefore become the quantities of choice in the quest for SHDM.

Let us now consider the circular and spherical harmonics again. Since a dipolar modulation may be explained (expected) in the UHECRs distribution by (from) scenarios other than the SHDM decay, we can look at the expected signal in higher harmonics. In Fig. 9 we show the one-dimensional c_2 (left) and two-dimensional C_2 (right) quadrupoles, for the reference case $N_{\rm ev}^{60}=300$. The quadrupoles are obviously not as sensitive as the dipoles, but their measurements would provide a useful cross-check on the SHDM model, because once the strength of the dipole is known we can automatically predict the strength of the quadrupole: these higher multipoles, even though less prominent, contain relevant pieces of information and can disentangle SHDM from other effects.

Finally, focussing again on the dipoles, we show in Fig. 10 how the expected sensitivities change when $N_{\rm ev}^{60}$ drops to 100. The peak sensitivities go from 1.5σ when $N_{\rm ev}^{60}=100$, to around (and above) 4σ for our baseline $N_{\rm ev}^{60}=300$ (and spike up to the $6\sigma-8\sigma$ with as many as 500 events, see Fig. 3. The peak sensitivities are once again reached around 100 EeV.

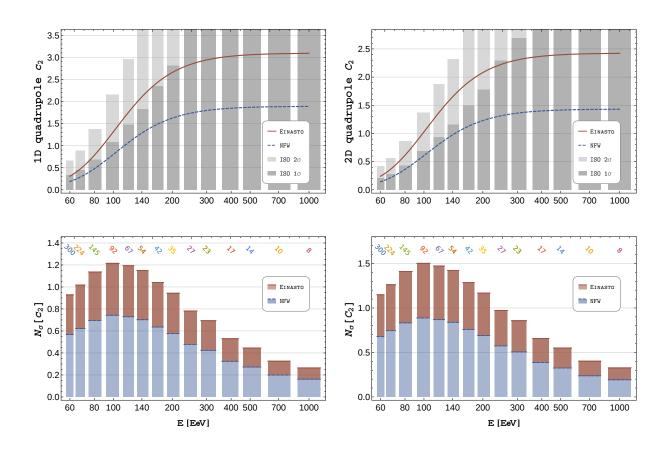


Figure 9: Performance of the 1D quadrupole c_2 (left) and 2D one C_2 (right) for $N_{\rm ev}^{60}=300$; see the text for details.

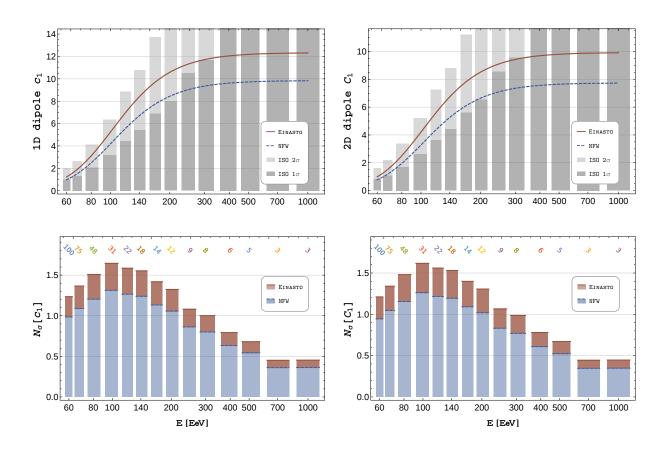


Figure 10: Performance of the 1D dipole c_1 (left) and 2D one C_1 (right) for $N_{\rm ev}^{60}=100$; see the text for details.

A. References

- [1] C. Patrignani et al. Review of Particle Physics. Chin. Phys., C40(10):100001, 2016.
- [2] Philip Bull et al. Beyond ACDM: Problems, solutions, and the road ahead. *Phys. Dark Univ.*, 12:56–99, 2016, 1512.05356.
- [3] Jihn E. Kim. Light Pseudoscalars, Particle Physics and Cosmology. *Phys. Rept.*, 150:1–177, 1987.
- [4] Yeong Gyun Kim, Kang Young Lee, and Seodong Shin. Singlet fermionic dark matter. *JHEP*, 05:100, 2008, 0803.2932.
- [5] Céline Boehm, Matthew J. Dolan, Christopher McCabe, Michael Spannowsky, and Chris J. Wallace. Extended gamma-ray emission from Coy Dark Matter. *JCAP*, 1405:009, 2014, 1401.6458.
- [6] Andi Hektor and Luca Marzola. Coy Dark Matter and the anomalous magnetic moment. *Phys. Rev.*, D90(5):053007, 2014, 1403.3401.
- [7] Pisin Chen and Ronald J. Adler. Black hole remnants and dark matter. *Nucl. Phys. Proc. Suppl.*, 124:103–106, 2003, gr-qc/0205106. [,103(2002)].
- [8] Paul H. Frampton, Masahiro Kawasaki, Fuminobu Takahashi, and Tsutomu T. Yanagida. Primordial Black Holes as All Dark Matter. *JCAP*, 1004:023, 2010, 1001.2308.
- [9] Eugeny Babichev, Luca Marzola, Martti Raidal, Angnis Schmidt-May, Federico Urban, Hardi Veermae, and Mikael von Strauss. Heavy spin-2 Dark Matter. JCAP, 1609(09):016, 2016, 1607.03497.
- [10] Eugeny Babichev, Luca Marzola, Martti Raidal, Angnis Schmidt-May, Federico Urban, Hardi Veermae, and Mikael von Strauss. Bigravitational origin of dark matter. *Phys. Rev.*, D94(8):084055, 2016, 1604.08564.
- [11] Katsuki Aoki and Shinji Mukohyama. Massive gravitons as dark matter and gravitational waves. *Phys. Rev.*, D94(2):024001, 2016, 1604.06704.
- [12] Gerard Jungman, Marc Kamionkowski, and Kim Griest. Supersymmetric dark matter. *Phys. Rept.*, 267:195–373, 1996, hep-ph/9506380.
- [13] Gianfranco Bertone, Dan Hooper, and Joseph Silk. Particle dark matter: Evidence, candidates and constraints. *Phys. Rept.*, 405:279–390, 2005, hep-ph/0404175.
- [14] Jennifer M. Gaskins. A review of indirect searches for particle dark matter. 2016, 1604.00014.
- [15] D. S. Akerib et al. Improved Limits on Scattering of Weakly Interacting Massive Particles from Reanalysis of 2013 LUX Data. *Phys. Rev. Lett.*, 116(16):161301, 2016, 1512.03506.

- [16] Vardan Khachatryan et al. Search for dark matter, extra dimensions, and unparticles in monojet events in proton–proton collisions at $\sqrt{s}=8$ TeV. Eur. Phys. J., C75(5):235, 2015, 1408.3583.
- [17] Georges Aad et al. Search for dark matter candidates and large extra dimensions in events with a jet and missing transverse momentum with the ATLAS detector. *JHEP*, 04:075, 2013, 1210.4491.
- [18] Georges Aad et al. Search for supersymmetry at \sqrt{s} =8 TeV in final states with jets and two same-sign leptons or three leptons with the ATLAS detector. *JHEP*, 06:035, 2014, 1404.2500.
- [19] Georges Aad et al. Search for supersymmetry using final states with one lepton, jets, and missing transverse momentum with the ATLAS detector in $\sqrt{s} = 7$ TeV pp. Phys. Rev. Lett., 106:131802, 2011, 1102.2357.
- [20] Serguei Chatrchyan et al. Search for Supersymmetry at the LHC in Events with Jets and Missing Transverse Energy. *Phys. Rev. Lett.*, 107:221804, 2011, 1109.2352.
- [21] Serguei Chatrchyan et al. Search for supersymmetry in hadronic final states with missing transverse energy using the variables α_T and b-quark multiplicity in pp collisions at $\sqrt{s}=8$ TeV. Eur. Phys. J., C73(9):2568, 2013, 1303.2985.
- [22] Daniel J. H. Chung, Edward W. Kolb, and Antonio Riotto. Superheavy dark matter. *Phys. Rev.*, D59:023501, 1999, hep-ph/9802238.
- [23] Vadim Kuzmin and Igor Tkachev. Ultrahigh-energy cosmic rays, superheavy long living particles, and matter creation after inflation. *JETP Lett.*, 68:271–275, 1998, hep-ph/9802304. [Pisma Zh. Eksp. Teor. Fiz.68,255(1998)].
- [24] Vadim Kuzmin and Igor Tkachev. Matter creation via vacuum fluctuations in the early universe and observed ultrahigh-energy cosmic ray events. *Phys. Rev.*, D59:123006, 1999, hep-ph/9809547.
- [25] Edward W. Kolb, Daniel J. H. Chung, and Antonio Riotto. WIMPzillas! In Trends in theoretical physics II. Proceedings, 2nd La Plata Meeting, Buenos Aires, Argentina, November 29-December 4, 1998, pages 91–105, 1998, hep-ph/9810361. [,91(1998)].
- [26] Vadim A. Kuzmin and Igor I. Tkachev. Ultrahigh-energy cosmic rays and inflation relics. *Phys. Rept.*, 320:199–221, 1999, hep-ph/9903542.
- [27] Edward W. Kolb, A. A. Starobinsky, and I. I. Tkachev. Trans-Planckian wimpzillas. *JCAP*, 0707:005, 2007, hep-th/0702143.
- [28] Chiaki Hikage, Kazuya Koyama, Takahiko Matsubara, Tomo Takahashi, and Masahide Yamaguchi. Limits on Isocurvature Perturbations from Non-Gaussianity in WMAP Temperature Anisotropy. *Mon. Not. Roy. Astron. Soc.*, 398:2188–2198, 2009, 0812.3500.
- [29] Daniel J. H. Chung and Hojin Yoo. Isocurvature Perturbations and Non-Gaussianity of Gravitationally Produced Nonthermal Dark Matter. *Phys. Rev.*, D87:023516, 2013, 1110.5931.

- [30] Daniel J. H. Chung, Lisa L. Everett, Hojin Yoo, and Peng Zhou. Gravitational Fermion Production in Inflationary Cosmology. *Phys. Lett.*, B712:147–154, 2012, 1109.2524.
- [31] Kristjan Kannike, Antonio Racioppi, and Martti Raidal. Super-Heavy Dark Matter Towards Predictive Scenarios from Inflation. 2016, 1605.09378.
- [32] Daniel J. H. Chung, Patrick Crotty, Edward W. Kolb, and Antonio Riotto. On the gravitational production of superheavy dark matter. *Phys. Rev.*, D64:043503, 2001, hep-ph/0104100.
- [33] R. Aloisio, S. Matarrese, and A. V. Olinto. Super Heavy Dark Matter in light of BICEP2, Planck and Ultra High Energy Cosmic Rays Observations. *JCAP*, 1508(08):024, 2015, 1504.01319.
- [34] Daniel J. H. Chung, Hojin Yoo, and Peng Zhou. Fermionic Isocurvature Perturbations. *Phys. Rev.*, D91(4):043516, 2015, 1306.1966.
- [35] Daniel J. H. Chung, Edward W. Kolb, Antonio Riotto, and Igor I. Tkachev. Probing Planckian physics: Resonant production of particles during inflation and features in the primordial power spectrum. *Phys. Rev.*, D62:043508, 2000, hep-ph/9910437.
- [36] S. L. Dubovsky and P. G. Tinyakov. Galactic anisotropy as signature of CDM related ultrahighenergy cosmic rays. *JETP Lett.*, 68:107–111, 1998, hep-ph/9802382.
- [37] Michael Kachelriess and D. V. Semikoz. Superheavy dark matter as UHECR source versus the SUGAR data. *Phys. Lett.*, B577:1–9, 2003, astro-ph/0306282.
- [38] Hang Bae Kim and Peter Tinyakov. Constraining superheavy dark matter model of UHECR with SUGAR data. *Astropart. Phys.*, 21:535–542, 2004, astro-ph/0306413.
- [39] Roberto Aloisio, V. Berezinsky, and M. Kachelriess. On the status of superheavy dark matter. *Phys. Rev.*, D74:023516, 2006, astro-ph/0604311.
- [40] R. Aloisio and F. Tortorici. Super Heavy Dark Matter and UHECR Anisotropy at Low Energy. *Astropart. Phys.*, 29:307–316, 2008, 0706.3196.
- [41] Karl-Heinz Kampert and Peter Tinyakov. Cosmic rays from the ankle to the cutoff. *Comptes Rendus Physique*, 15:318–328, 2014, 1405.0575.
- [42] Denis Allard. Extragalactic propagation of ultrahigh energy cosmic-rays. *Astropart. Phys.*, 39-40:33–43, 2012, 1111.3290.
- [43] Antoine Letessier-Selvon and Todor Stanev. Ultrahigh Energy Cosmic Rays. *Rev. Mod. Phys.*, 83:907–942, 2011, 1103.0031.
- [44] Kenneth Greisen. End to the cosmic ray spectrum? Phys. Rev. Lett., 16:748-750, 1966.
- [45] G. T. Zatsepin and V. A. Kuzmin. Upper limit of the spectrum of cosmic rays. *JETP Lett.*, 4:78–80, 1966. [Pisma Zh. Eksp. Teor. Fiz.4,114(1966)].

- [46] Kumiko Kotera and Angela V. Olinto. The Astrophysics of Ultrahigh Energy Cosmic Rays. *Ann. Rev. Astron. Astrophys.*, 49:119–153, 2011, 1101.4256.
- [47] Subir Sarkar and Ramon Toldra. The High-energy cosmic ray spectrum from relic particle decay. *Nucl. Phys.*, B621:495–520, 2002, hep-ph/0108098.
- [48] R. Aloisio, V. Berezinsky, and M. Kachelriess. Fragmentation functions in SUSY QCD and UHECR spectra produced in top - down models. *Phys. Rev.*, D69:094023, 2004, hep-ph/0307279.
- [49] Rahul Basu and Pijushpani Bhattacharjee. On the injection spectrum of ultrahigh energy cosmic rays in the top down scenario. *Phys. Rev.*, D70:023510, 2004, hep-ph/0403299.
- [50] Yuri L. Dokshitzer. Calculation of the Structure Functions for Deep Inelastic Scattering and e+ e- Annihilation by Perturbation Theory in Quantum Chromodynamics. *Sov. Phys. JETP*, 46:641–653, 1977. [Zh. Eksp. Teor. Fiz.73,1216(1977)].
- [51] V. N. Gribov and L. N. Lipatov. Deep inelastic e p scattering in perturbation theory. *Sov. J. Nucl. Phys.*, 15:438–450, 1972. [Yad. Fiz.15,781(1972)].
- [52] L. N. Lipatov. The parton model and perturbation theory. *Sov. J. Nucl. Phys.*, 20:94–102, 1975. [Yad. Fiz.20,181(1974)].
- [53] Guido Altarelli and G. Parisi. Asymptotic Freedom in Parton Language. *Nucl. Phys.*, B126:298–318, 1977.
- [54] Guillaume Decerprit and Denis Allard. Constraints on the origin of ultrahigh energy cosmic rays from cosmogenic neutrinos and photons. *Astron. Astrophys.*, 535:A66, 2011, 1107.3722.
- [55] Guenter Sigl. High Energy Neutrinos and Cosmic Rays. *Proc. Int. Sch. Phys. Fermi*, 182:145–184, 2012, 1202.0466.
- [56] J. Alvarez-Muniz, M. Risse, G. I. Rubtsov, and B. T. Stokes. Review of the Multimessenger Working Group at UHECR-2012. *EPJ Web Conf.*, 53:01009, 2013, 1306.4199.
- [57] Dmitri Ivanov. TA Spectrum Summary. PoS, ICRC2015:349, 2016.
- [58] T. Abu-Zayyad et al. The Energy Spectrum of Ultra-High-Energy Cosmic Rays Measured by the Telescope Array FADC Fluorescence Detectors in Monocular Mode. *Astropart. Phys.*, 48:16–24, 2013, 1305.6079.
- [59] T. Abu-Zayyad et al. The Cosmic Ray Energy Spectrum Observed with the Surface Detector of the Telescope Array Experiment. *Astrophys. J.*, 768:L1, 2013, 1205.5067.
- [60] Ines Valino. The flux of ultra-high energy cosmic rays after ten years of operation of the Pierre Auger Observatory. *PoS*, ICRC2015:271, 2016.
- [61] Alexander Aab et al. Measurement of the cosmic ray spectrum above 4 imes 10¹⁸ eV us-

- ing inclined events detected with the Pierre Auger Observatory. *JCAP*, 1508:049, 2015, 1503.07786.
- [62] P. A. R. Ade et al. Planck 2015 results. XIII. Cosmological parameters. *Astron. Astrophys.*, 594:A13, 2016, 1502.01589.
- [63] Paolo Gondolo, Graciela Gelmini, and Subir Sarkar. Cosmic neutrinos from unstable relic particles. *Nucl. Phys.*, B392:111–136, 1993, hep-ph/9209236.
- [64] G. I. Rubtsov, M. Fukushima, D. Ivanov, M. S. Piskunov, B. Stokes, G. Thomson, and S. V. Troitsky. Telescope Array search for photons and neutrinos with the surface detector data. *PoS*, ICRC2015:331, 2016.
- [65] J. Abraham et al. Upper limit on the cosmic-ray photon flux above 10¹⁹ eV using the surface detector of the Pierre Auger Observatory. *Astropart. Phys.*, 29:243–256, 2008, 0712.1147.
- [66] J. Abraham et al. Upper limit on the cosmic-ray photon fraction at EeV energies from the Pierre Auger Observatory. *Astropart. Phys.*, 31:399–406, 2009, 0903.1127.
- [67] V. Scherini. Search for ultra-high energy photons at the Pierre Auger Observatory. *EPJ Web Conf.*, 53:05002, 2013.
- [68] Carla Bleve. Updates on the neutrino and photon limits from the Pierre Auger Observatory. *PoS*, ICRC2015:1103, 2016.
- [69] Marco Cirelli, Gennaro Corcella, Andi Hektor, Gert Hutsi, Mario Kadastik, Paolo Panci, Martti Raidal, Filippo Sala, and Alessandro Strumia. PPPC 4 DM ID: A Poor Particle Physicist Cookbook for Dark Matter Indirect Detection. *JCAP*, 1103:051, 2011, 1012.4515. [Erratum: JCAP1210,E01(2012)].
- [70] J. Einasto. On the Construction of a Composite Model for the Galaxy and on the Determination of the System of Galactic Parameters. *Trudy Astrofizicheskogo Instituta Alma-Ata*, 5:87–100, 1965.
- [71] Julio F. Navarro, Carlos S. Frenk, and Simon D. M. White. The Structure of cold dark matter halos. *Astrophys. J.*, 462:563–575, 1996, astro-ph/9508025.
- [72] Alexander Aab et al. Searches for Large-Scale Anisotropy in the Arrival Directions of Cosmic Rays Detected above Energy of 10¹⁹ eV at the Pierre Auger Observatory and the Telescope Array. *Astrophys. J.*, 794(2):172, 2014, 1409.3128.
- [73] Olivier Deligny. Large-Scale Distribution of Arrival Directions of Cosmic Rays Detected at the Pierre Auger Observatory and the Telescope Array above 10¹⁹ eV. *PoS*, ICRC2015:395, 2016.
- [74] P. Sommers. Cosmic ray anisotropy analysis with a full-sky observatory. *Astropart. Phys.*, 14:271–286, 2001, astro-ph/0004016.

- [75] M. S. Pshirkov, P. G. Tinyakov, and F. R. Urban. New limits on extragalactic magnetic fields from rotation measures. *Phys. Rev. Lett.*, 116(19):191302, 2016, 1504.06546.
- [76] Alex Zucca, Yun Li, and Levon Pogosian. Constraints on Primordial Magnetic Fields from Planck combined with the South Pole Telescope CMB B-mode polarization measurements. 2016, 1611.00757.
- [77] Foteini Oikonomou, Kumiko Kotera, and Filipe B. Abdalla. Simulations for a next-generation UHECR observatory. *JCAP*, 1501(01):030, 2015, 1409.1925.
- [78] B. Rouillé d'Orfeuil, D. Allard, C. Lachaud, E. Parizot, C. Blaksley, and S. Nagataki. Anisotropy expectations for ultra-high-energy cosmic rays with future high statistics experiments. *Astron. Astrophys.*, 567:A81, 2014, 1401.1119.
- [79] Eli Waxman. Cosmological origin for cosmic rays above 10**19-eV. *Astrophys. J.*, 452:L1–L4, 1995, astro-ph/9508037.